SCIENTIFIC REPORTS

OPEN

In-situ synthesis of amorphous silver silicate/carbonate composites for selective visible-light photocatalytic decomposition

Received: 21 July 2017
Accepted: 24 October 2017
Published online: 08 November 2017

Ruya Cao, Hongcen Yang, Xiaolong Deng, Shouwei Zhang & Xijin Xu

Coupling two different semiconductors to form composite photocatalysts is an extremely significant technique for environmental remediation. Here, a one-step *in-situ* precipitation method has been developed to prepare amorphous silver silicate/carbonate ($AgSiO/Ag_2CO_3$) nanoparticles (NPs) composites, which are well dispersed sphere-like particles with the sizes of around ~50–100 nm. The high-efficiency photocatalytic activities under visible light (VL) have been carefully evaluated, and the $AgSiO/Ag_2CO_3$ NPs composites exhibit selective photocatalytic degradations on Methylene Blue (MB) and Rhodamine B (RhB). The maximum degradation rate for MB can reach ~99.1% within ~40 min under VL irradiation, much higher than that of RhB (~12%) in the same condition, which can be ascribed to (I) the smaller molecule size of MB than that of RhB, (II) the fast charge separation between AgSiO NPs and Ag_2CO_3 NPs, abundant heterojunction interfaces as well as fully exposed reactive sites. These composites are proposed to be an example for the preparation of other silicate composite photocatalysts for practical applications in environmental remediation.

Photocatalytic technology has become one of the most promising green technology as it can degrade organic pollutants in water to produce non-toxic substances such as CO_2, H_2O and so on with no secondary pollution, mild reaction conditions, and low energy consumption[1–3]. Especially, semiconductor photocatalysts have attracted wide attention in the field of environmental purification and a lot of achievements have been achieved[4,5]. Among them, silver carbonate (Ag_2CO_3) has received great research interests, but is restricted by its photocorrosion and lower photocatalytic degradation efficiency[2]. Therefore, it is significantly worthy to make great efforts to solve the problem for the real industrial application. Recently, it has been reported that introducing an electron acceptor in the photocatalytic reaction system can efficiently restrain the photocorrosion[3]. The silicates have been found to be the effective one[6,7], which can not only enhance the photogenerated charge transfer but also broaden the spectral response range[6–8]. Furthermore, the excited electron–hole pairs can readily transfer between the particles due to the internal polar electric field in the silicate NPs. Among them, silver silicate (AgSiO) has been one of the most famous silicates due to its good stability, high efficiency, nontoxicity, low cost, and it has row band gap which can extend the large of light absorption[8]. Therefore, visible-light-driven photocatalysts can be exploited by coupling AgSiO with Ag_2CO_3 NPs. Furthermore, the heterojunctions by coupling them favor the separation of photogenerated electron-hole pairs resulting in the improvement of the photocatalytic activity[9,10].

In this paper, $AgSiO/Ag_2CO_3$ composites with different ratios have been successfully synthesized by an *in-situ* method. The final samples with different molar ratios of SiO_3^{2-} and CO_3^{2-} exhibit the optimal photocatalytic activities. Besides, the selective photodegradation of two cationic dyes Methylene Blue (MB), Rhodamine B (RhB), and two another anionic dyes Methyl Orange (MO) and Congo Red (Cr) have been carefully investigated[11]. Finally, the photocatalytic mechanisms of these $AgSiO/Ag_2CO_3$ composites are carefully discussed.

Experimental Sections

Preparation of the amorphous silver silicates (AgSiO). The AgSiO was synthesized via an *in-situ* method. For a typical synthesis, 0.2 M $AgNO_3$ (40 mL) was added into 0.1 M $Na_2SiO_3{\cdot}9H_2O$ (40 mL) under

School of Physics and Technology, University of Jinan, Shandong, 250022, P.R. China. Correspondence and requests for materials should be addressed to S.Z. (email: zhangsw-1122@163.com) or X.X. (email: sps_xuxj@ujn.edu.cn)

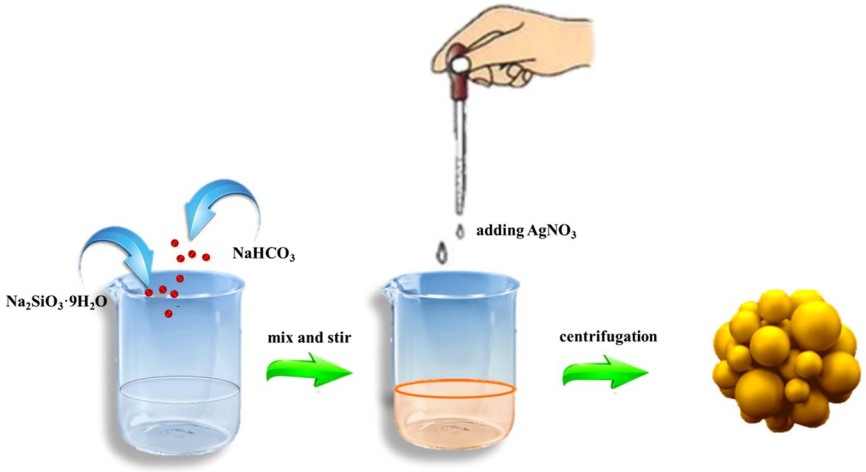

Figure 1. Schematic illustration of the synthesis of $AgSiO/Ag_2CO_3$ composites.

continuously stirring for 1.0 h. The precipitates were collected and washed with distilled water and ethanol, and finally dried at room temperature.

Preparation of the silver carbonate (Ag_2CO_3). 0.2 M $AgNO_3$ (40 mL) was slowly drop by drop added into 0.1 M $NaHCO_3$ (20 mL) under continuously stirring for 1.0 h. The precipitates were collected and washed with distilled water and ethanol, and finally dried at room temperature.

Preparation of the amorphous silver silicate/carbonate heterostructure ($AgSiO/Ag_2CO_3$). The $AgSiO/Ag_2CO_3$ composites were synthesized via an *in-situ* precipitation method. In a typical synthetic procedure, 0.1 M $Na_2SiO_3{\cdot}9H_2O$ (40 mL) were added to 0.1 M $NaHCO_3$ (20 mL) under stirring for 5 min. Then, 0.2 M $AgNO_3$ (40 mL) was slowly added to the mixture under stirring for 1.0 h. The precipitates were collected and washed with distilled water and ethanol, and dried at room temperature. The $AgSiO/Ag_2CO_3$ composites prepared with different molar ratios of $Na_2SiO_3{\cdot}9H_2O$ and $NaHCO_3$ in 40, 60, 80, 100 and 120 ml are denominated as $AgSiO/Ag_2CO_3$-2:1, $AgSiO/Ag_2CO_3$-3:1, $AgSiO/Ag_2CO_3$-4:1, $AgSiO/Ag_2CO_3$-5:1, and $AgSiO/Ag_2CO_3$-6:1, respectively.

Characterization. Powder X-ray diffraction (XRD) patterns were collected using a D/MAX2500 V diffractometer equipped with Cu K_α radiation ($\lambda = 1.5418$ Å). The morphologies of the materials were observed using a FEI QUANTA FEG 250 field emission scanning electron microscope (SEM). The structural information of the samples was measured with the standard KBr disk method by a Fourier transform spectrophotometer (FT-IR, Avatar 370, thermo Nicolet). X-ray photoelectron spectroscopy (XPS) was carried out on ESCALAB250 with Mg K_α as the source and the C_{1s} peak at 284.6 eV as an internal standard. UV-vis diffuse reflection spectroscopy (DRS) was recorded with a Shimadzu UV-2500 spectrophotometer using $BaSO_4$ as the reference. The Brunauer–Emmett–Teller (BET) specific surface areas were explored by nitrogen adsorption in a Micromeritics Tristar II 3020 nitrogen adsorption–desorption apparatus in accordance with the Barret–Joyner–Halenda (BJH) technique from the N_2 adsorption isotherms.

Photocatalytic tests. Photocatalytic degradation experiments were conducted in a photocatalytic reactor equipped with a 420 nm cut-off filter and a 500 W Xe lamp as the light source. For the photocatalytic reaction, the photocatalysts (20 mg) were mixed into a MB and RhB solution (50 mL, 10 mg/L). To guarantee the adsorption-desorption counterpoise, the mixed solution was stirred for 60 min in the darkness. Then, the solution was illuminated by VL and a small portion of the suspension (~3.0 mL) was sampled at 10 min illumination spacing. The catalytic efficiency was tested by using a UV-vis spectrophotometer (UV-2500, Shimadzu) for the degradation of RhB and MB.

Results and Discussion

A facile *in-situ* precipitation method was designed to synthesize $AgSiO/Ag_2CO_3$ nanoparticles as illustrated in Fig. 1. The chemical reaction process can be described as follows:

$$Ag^+ + SiO_3^{2-} + CO_3^{2-} + OH^- \rightarrow AgSiO/Ag_2CO_3 + H_2O \quad (1)$$

By adding $AgNO_3$ to the $NaHCO_3$ solution, the CO_3^{2-} present in the solution will react with the added Ag^+ by electrostatic interaction to produce Ag_2CO_3. Then, the fixed Ag^+ cations will further react with SiO_3^{2-} to generate AgSiO with the addition of Na_2SiO_3 solution, resulting in the formation of $AgSiO/Ag_2CO_3$[5–7].

The XRD patterns of pure AgSiO, Ag_2CO_3 and $AgSiO/Ag_2CO_3$ composites are shown in Fig. 2. The broad peak at about 34° could be indexed to the (−124) and (−115) planes for pure AgSiO in Fig. 2A, suggesting its amorphous structure[6]. For the pure Ag_2CO_3 NPs (Fig. 2B), the positions and intensities of the diffraction peaks are well matched with the standard JCPDS card[2,3,11]. The XRD pattern of $AgSiO/Ag_2CO_3$ composites is shown in Fig. 2A. Obviously, the diffraction peaks of AgSiO and Ag_2CO_3 NPs can be clearly found in curve and without any other

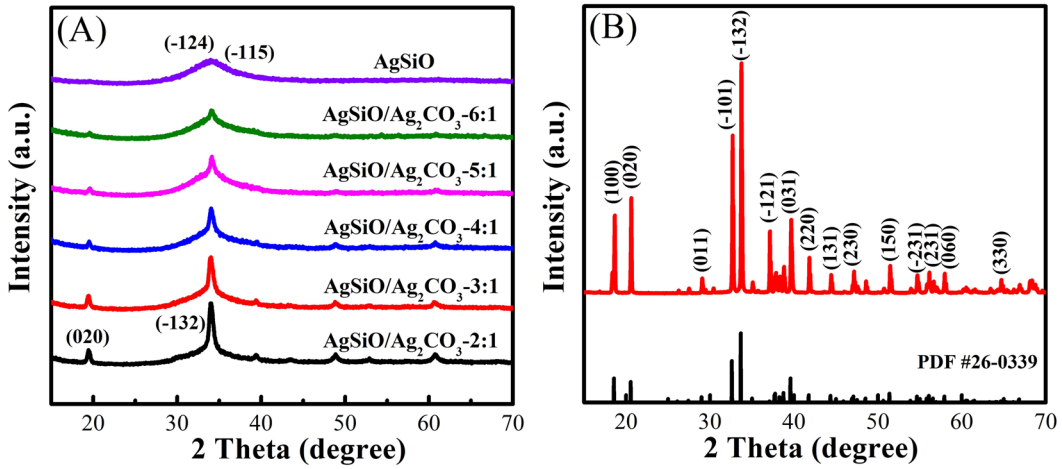

Figure 2. XRD patterns of (**A**) pure AgSiO and AgSiO/Ag_2CO_3 composites, (**B**) pure Ag_2CO_3.

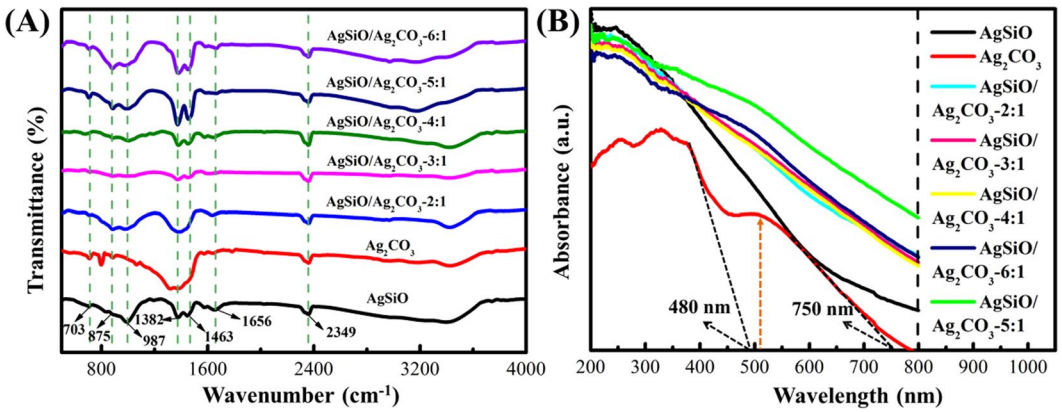

Figure 3. (**A**) FT-IR spectras of pure Ag_2CO_3, AgSiO and AgSiO/Ag_2CO_3 composites; (**B**) UV-vis diffuses reflectance spectra of Ag_2CO_3, AgSiO and AgSiO/Ag_2CO_3 composites.

peaks. The peaks of Ag_2CO_3 decreased with increasing AgSiO contents, and the characteristic peak intensity of AgSiO increases with the increase of the AgSiO contents, indicating that AgSiO/Ag_2CO_3 composites with high purity have been successfully synthesized by an *in-situ* precipitation[1,8].

FTIR spectra of AgSiO, Ag_2CO_3 and AgSiO/Ag_2CO_3 composites were recorded as shown in Fig. 3. In comparison to pure AgSiO, the absorption bands of AgSiO/Ag_2CO_3 composites obtained at around ~705 cm^{-1}, ~893 cm^{-1}, ~1382 cm^{-1}, and ~1451 cm^{-1} are attributed to CO_3^{2-} in Ag_2CO_3[1,10]. Compared with pure Ag_2CO_3, strong absorption band at around ~1382 cm^{-1} is found for AgSiO/Ag_2CO_3 composites, which belongs to the Si-O-Si stretching vibrations[8]. Moreover, there is also another shoulder peak indexed to the Si-O-Si bonds at ~1630 cm^{-1}, which confirms the successful introduction of AgSiO in the composites. Nevertheless, the characteristic peak located at ~1382 cm^{-1} shifts to higher wavenumbers (Fig. 3). The observed blue shift in the composites after introducing AgSiO (Fig. 3) indicates the weakened bond strengths of Si-O-Si owing to the conjugation between Ag_2CO_3 and AgSiO[8,12]. This result demonstrates the strong interfacial coupling effect in the AgSiO/Ag_2CO_3 composites. Compared with the aggregated or large-size nanoparticles, the nature of AgSiO nanoparticles on Ag_2CO_3 acted as nano-islands can facilitate the formation of the heterojunction interfaces and guarantee the higher contact areas[13,14]. Both characters are essentials to promote photocatalytic activity and to enhance the separation efficiency of photogenerated charges.

The UV-vis diffuse reflectance spectra of AgSiO/Ag_2CO_3 composites together with pure AgSiO and Ag_2CO_3 are shown in Fig. 3. The light absorption edge of Ag_2CO_3 is measured to be ~480 nm, and mainly absorptions are ultraviolet light[14]. In addition, the peak at 520 nm can be indexed to the Ag nanocrystals. Therefore, we can see that a broad absorption ranging from ~480 to ~750 nm is detected, which is due to the generation of Ag nanocrystals[15,16]. The AgSiO/Ag_2CO_3 composites exhibit the stronger absorption than that of the Ag_2CO_3 NPs in both the visible and ultraviolet light region[17]. Obviously, the introduction of AgSiO can significantly enhance the absorption in the visible-light region and can even extend to near-infrared region, which is attributed to the SPR of Ag nanoparticles. It is inferred that the heterojunction of AgSiO/Ag_2CO_3 composites results in significantly

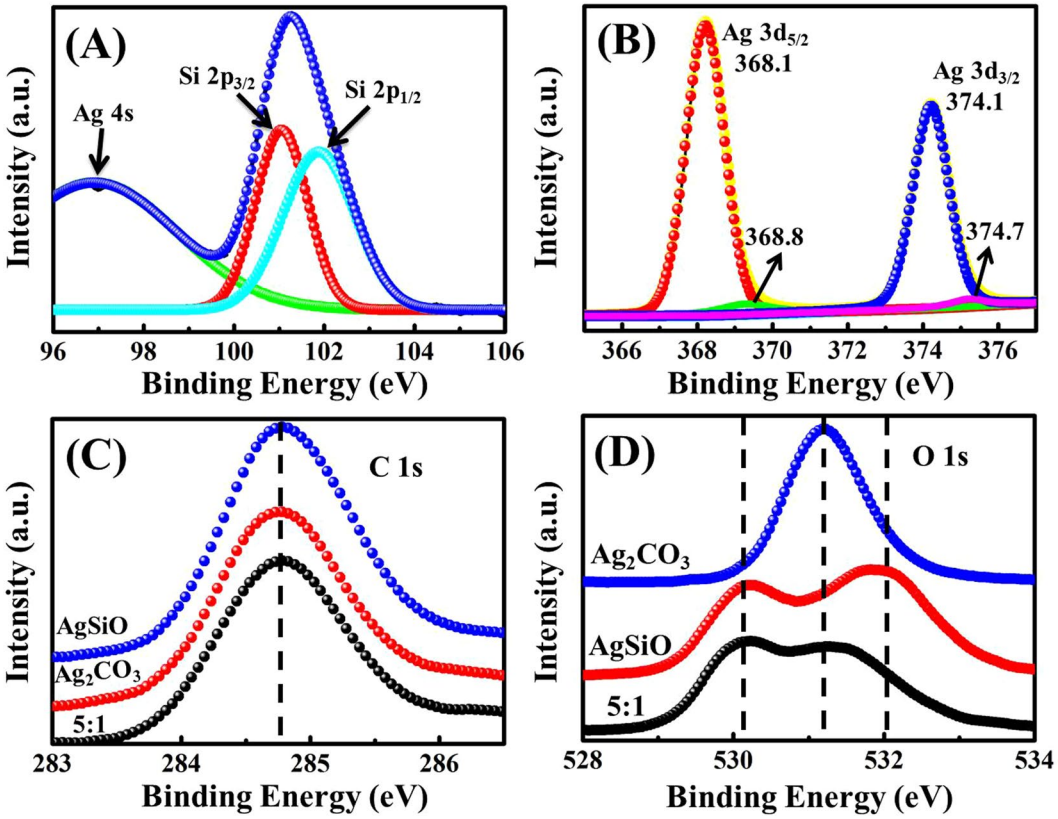

Figure 4. (**A**,**B**) main peaks of Si $2p_{3/2}$, Si $2p_{1/2}$ and Ag 3d for the AgSiO/Ag_2CO_3-5:1 composite; (**C**,**D**) high-resolution XPS spectra of C 1 s and O 1 s of the pure AgSiO, Ag_2CO_3 and AgSiO/Ag_2CO_3-5:1 composite.

decreased interfacial contact barrier and strengthened electronic coupling of the semiconductors to generate more photogenerated electrons/holes with improved photocatalytic performance[18,19].

The surface chemical compositions of AgSiO, Ag_2CO_3 and AgSiO/Ag_2CO_3-5:1 composite were investigated by XPS (Fig. 4). The full-scan XPS spectra of pure AgSiO, Ag_2CO_3 and AgSiO/Ag_2CO_3-5:1 composite (Figure S1) indicate the presence of Ag, Si, O in AgSiO, Ag, C, O in Ag_2CO_3 and Ag, Si, O, C in AgSiO/Ag_2CO_3-5:1 composite, respectively[15]. Figure 4A depictes the Si 2p peak of AgSiO/Ag_2CO_3-5:1 composite. The divided peaks located at ~96.9, ~102.8 and ~101 eV can be indexed into Ag 4 s, Si $2p_{1/2}$ and Si $2p_{3/2}$, respectively[6]. Figure 4B shows two XPS peaks located at ~368.1 eV and ~374.1, which can be indexed to Ag $3d_{5/2}$ and Ag $3d_{3/2}$ of pure AgSiO, Ag_2CO_3 and the AgSiO/Ag_2CO_3-5:1 composite[16,17]. These two peaks can be further divided into four peaks, ~368.1 and ~374.1 eV for Ag^+ $3d_{5/2}$ and $3d_{3/2}$, and ~368.8 and ~374.7 eV for Ag^0 $3d_{5/2}$ and $3d_{3/2}$, respectively. The peaks at ~368.8 and ~374.7 eV confirm the existence of metallic Ag^0 in our AgSiO/Ag_2CO_3-5:1 composite. The carbon element in AgSiO is mostly ascribed to the adventitious hydrocarbon from XPS itself. Therefore the strength of C 1 s obeys the decreasing order of Ag_2CO_3 > AgSiO/Ag_2CO_3 > AgSiO[20]. Figure 4D demonstrates that O 1 s peak in AgSiO/Ag_2CO_3 contains two distinguishable shoulders in the spectrum, demonstrating that two chemical states of oxygen are present on the surface[21]. The O 1 s peak at ~530.18 eV can be ascribed to O in AgSiO. Another peak at ~531.93 eV is attributed to O in AgSiO and Ag_2CO_3[19].

The morphologies of Ag_2CO_3, AgSiO and AgSiO/Ag_2CO_3 with different ratios are shown Fig. 5. It can be observed that Ag_2CO_3 are composed of microcubes with the length of ~1.0–5.0 μm in Fig. 5A[22]. Figure 5B clearly shows that the AgSiO samples are sphere-like particles with the sizes of ~50–100 nm[22,23]. Figure 5C–F indicate that the morphologies of AgSiO/Ag_2CO_3 with different ratios are similar to AgSiO[24]. The presence of SiO^{2-} in the sources has great effects on the final morphology of composite. The particle sizes of the composite decrease with the increase addition of SiO^{2-}. Furthermore, most particles are non-agglomerated and the sizes are mostly less than 100 nm, demonstrating that the samples are really nanosized cluster compounds[24]. The intimate contact between AgSiO and Ag_2CO_3 will strengthen the photogenerated charge separation and transfer[25]. Compared with traditional aggregated or large contact structures, this AgSiO/Ag_2CO_3 composites can not only provide more surface active sites for sequential photocatalytic reactions, but also shorten the migration distance of photogenerated charges[10].

The HRTEM images in Figure S2(A,B) show that the size of AgSiO/Ag_2CO_3 NPs is of 10 to 20 nm. The lattices of AgSiO/Ag_2CO_3 NPs are clearly visible in the HRTEM images. The close interface between the AgSiO and Ag_2CO_3 nanoparticles reveals the formation of nano-heterojunction[26]. From the figure, we can see that Ag_2CO_3 is uniformly packaged by an amorphous AgSiO, limiting the growth of Ag_2CO_3[27]. Figure S2(B) shows the lattice spacing of uniformly dispersed Ag_2CO_3 nanoparticles. The lattice fringes of 0.275 nm is in agreement with the

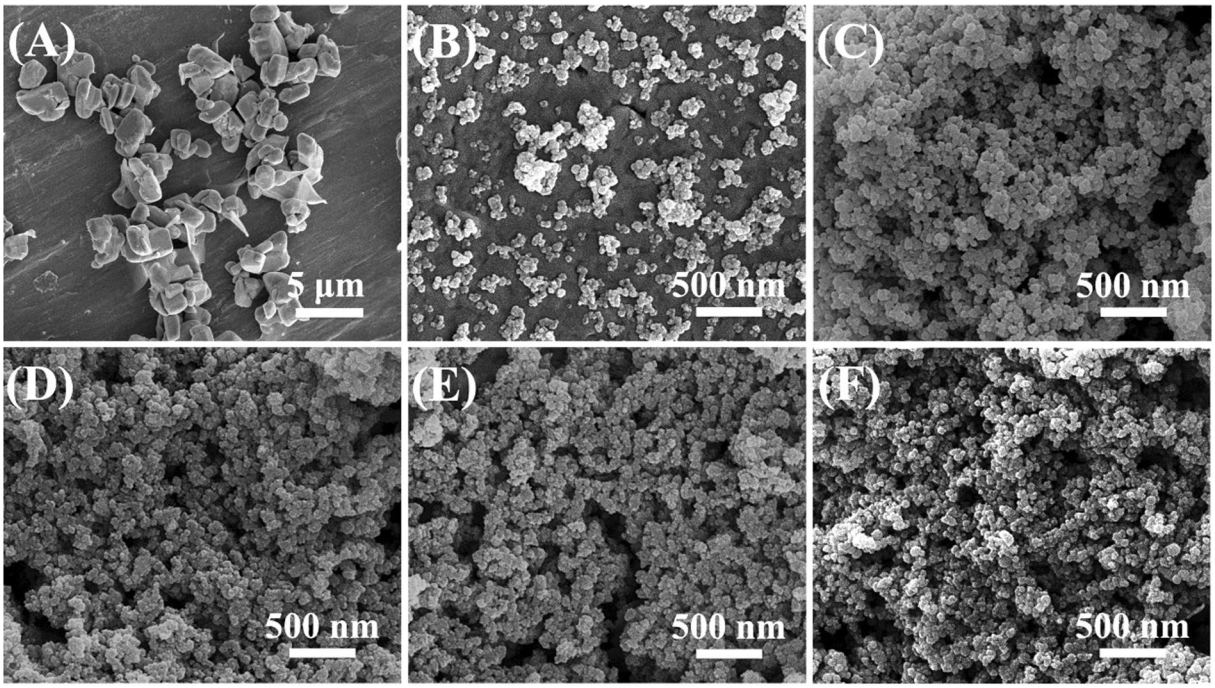

Figure 5. SEM images of (**A**) pure Ag_2CO_3, (**B**) pure AgSiO, (**C**) AgSiO/Ag_2CO_3-3:1 composite, (**D**) AgSiO/Ag_2CO_3-4:1 composite, (**E**) AgSiO/Ag_2CO_3-5:1 composite and (**F**) AgSiO/Ag_2CO_3-6:1 composite.

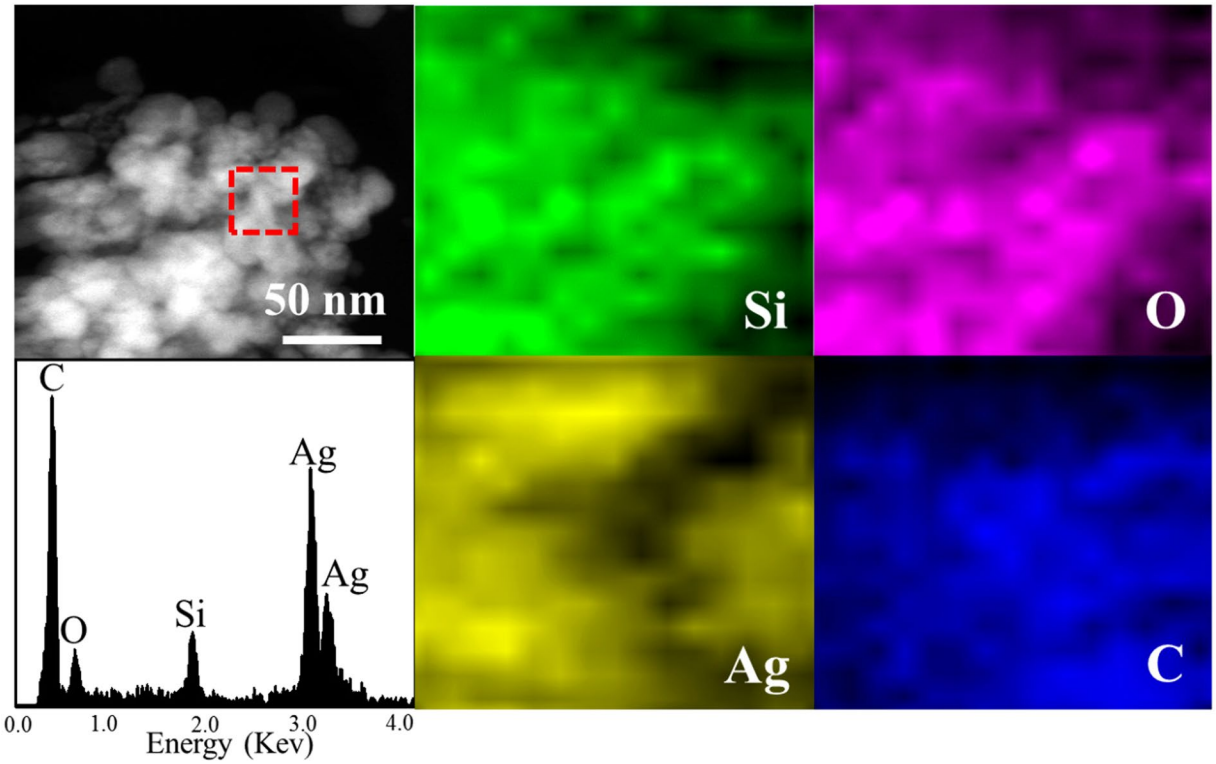

Figure 6. Elemental mapping images and EDS spectrum of the AgSiO/Ag_2CO_3-5:1 composite.

spacings of the (−101) plane of Ag_2CO_3 and consistent with JCPDS Card No. 26–0339[28]. No lattice fringes of AgSiO can be observed. This kind of heterojunction, which is favorable for the transport of photoexcited carriers, is formed between AgSiO and Ag_2CO_3[29]. Mainwhile, the composites can be further characterized by element mapping and EDS images (Fig. 6), where the Ag, Si, O and C elements are homogeneously distributed over the

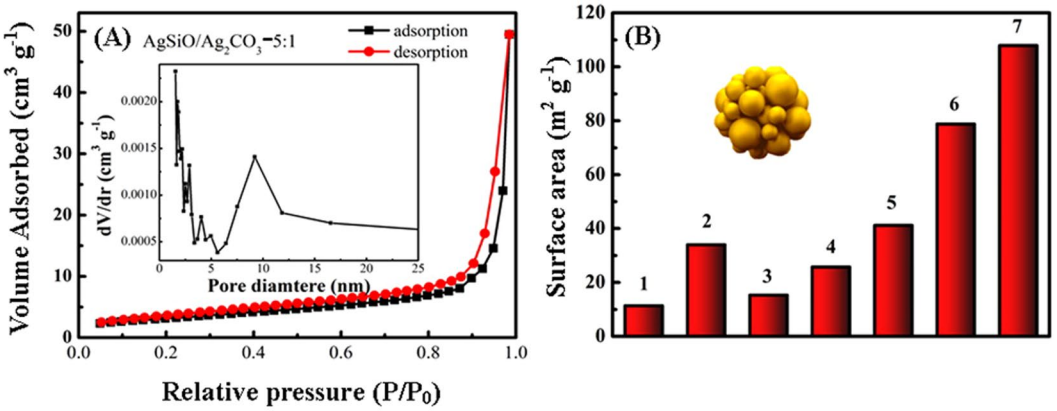

Figure 7. (**A**) N_2 adsorption–desorption is otherms and pore size distribution curves calculated for AgSiO/Ag_2CO_3-5:1 composite; (**B**) surface area values of (1) Ag_2CO_3, (2) AgSiO, (3) AgSiO/Ag_2CO_3-2:1 composite,(4) AgSiO/Ag_2CO_3-3:1 composite, (5) AgSiO/Ag_2CO_3-4:1 composite, (6) AgSiO/Ag_2CO_3-5:1 composite and (7) AgSiO/Ag_2CO_3-6:1 composite.

whole profile[30–32]. From the above results, we can expect that the strong interfacial coupling effect between AgSiO and Ag_2CO_3 will promote photogenerated electron-hole pairs separation and transfer, and thus further enhance the photocatalytic performance of AgSiO/Ag_2CO_3 composites[33].

Surface area, pore size and pore volume parameters for pure AgSiO, pure Ag_2CO_3 and AgSiO/Ag_2CO_3 composites were also investigated. The porosity of the AgSiO/Ag_2CO_3 composites sample is clearly enhanced. According to Figure S3, all the materials except for Ag_2CO_3 show a narrow pore size distribution with the average diameter of $d > 2$ nm[13,34]. With further increase of the AgSiO content, the adsorbed volume drops obviously indicating that the enhancement in adsorption volume is not driven solely by the small particles[6,13,35]. The surface areas of the different AgSiO/Ag_2CO_3 composites and pure AgSiO and Ag_2CO_3 are also calculated as shown in Fig. 7B for a better understanding of the composite nanostructure. It can be seen that the surface area of Ag_2CO_3 is ~11.4 $m^2 \cdot g^{-1}$. With further increasing of the amount of the AgSiO, the surface area values of the AgSiO/Ag_2CO_3 composites increase obviously. The surface area of AgSiO/Ag_2CO_3-6:1 composite can be achieved ~107.9 $m^2 \cdot g^{-1}$. Although the AgSiO/Ag_2CO_3-5:1 composite specific surface area isn't the largest, the degradation is best, which can be attributed to its heterogeneous structure.

Photocatalytic tests. The photocatalytic activities of pure AgSiO, Ag_2CO_3 and AgSiO/Ag_2CO_3 composites with different ratios under VL irradiation are shown in Fig. 8. The degradation reaches as ~99.1% under VL irradiation within ~40 min (Fig. 8A,B). The degradation of RhB is only ~12% in the same condition (Fig. 8C,D)[36,37].

All AgSiO/Ag_2CO_3 composites exhibit higher photocatalytic activities than either AgSiO or Ag_2CO_3 with the order of AgSiO/Ag_2CO_3-5:1 > AgSiO/Ag_2CO_3-6:1 > AgSiO/Ag_2CO_3-4:1 > AgSiO/Ag_2CO_3-3:1 > AgSiO/Ag_2CO_3-2:1 > AgSiO > Ag_2CO_3, indicating the positive effect of AgSiO contents on enhancing the photocatalytic activities of the composites[8,37]. Full degradation of MB can be observed within ~40 min by VL irradiation in the presence of AgSiO/Ag_2CO_3-5:1 composite (Fig. 8A), illustrating the significantly improved photocatalytic activity of the AgSiO/Ag_2CO_3 composites[36]. However, further increment of proportion (AgSiO/Ag_2CO_3-6:1) results in decreased photocatalytic activity, which may be attributed to the recombination of photogenerated electrons and holes, and thenthe photocatalytic efficiency is restrained[38].

Figure 9 shows the variation of the absorption spectra of MB under VL irradiation by AgSiO/Ag_2CO_3-5:1 composite. The characteristic peak intensities of MB gradually decrease by prolonging the irradiation time, and the adsorption peaks disappear within ~40 min irradiation[12,39]. The corresponding optical photographs of MB degradation using different photocatalysts under different irradiation times are collected and displayed in Fig. 9B. The color of MB gradually becomes lighter by prolonging the irradiation time, it can be seen that the color of AgSiO/Ag_2CO_3-5:1 composite becomes transparent while pure color for AgSiO and Ag_2CO_3 turns into azury[40]. The variation of the absorption spectra of RhB under VL irradiation by AgSiO/Ag_2CO_3-5:1 composite is shown in Fig. 9C. The characteristic peak intensities of RhB gradually decreased by prolonging the irradiation time, and the adsorption peaks became constant within ~40 min irradiation indicating the very slow degradation of RhB[12,38]. These corresponding optical photographs of RhB degradation using different photocatalysts under different irradiation times are in Fig. 9D, showing that the color of RhB almost keeps unchanged.

The selective photocatalytic phenomenon of the AgSiO/Ag_2CO_3-5:1 composite was examined by photodegradation of MB and RhB[38]. The absorptions peaks of MB located at ~664 nm almost disappear after irradiation within ~40 min. However, the absorption peaks of RhB located at ~554 nm doesn't change too much (Fig. 9)[39]. As for two cationic dyes MB and RhB, we speculate that the discrepancy in adsorption capacities among them can be ascribed to the molecule size[29,35]. That is, because the size of MB molecules is smaller than those of RhB, MB can be intercalated into the space, while RhB are too large to intercalate into the NPs[37].

Similarly, we used MB&MO, MO&RhB and MO&CR mixture dyes to further research the selectivity of the material. As shown from the figure S4, When AgSiO/Ag_2CO_3 composites were added into the binary mixtures, respectively, the characteristic peaks of cationic dyes MB disappeared quickly, while the characteristic peaks of all

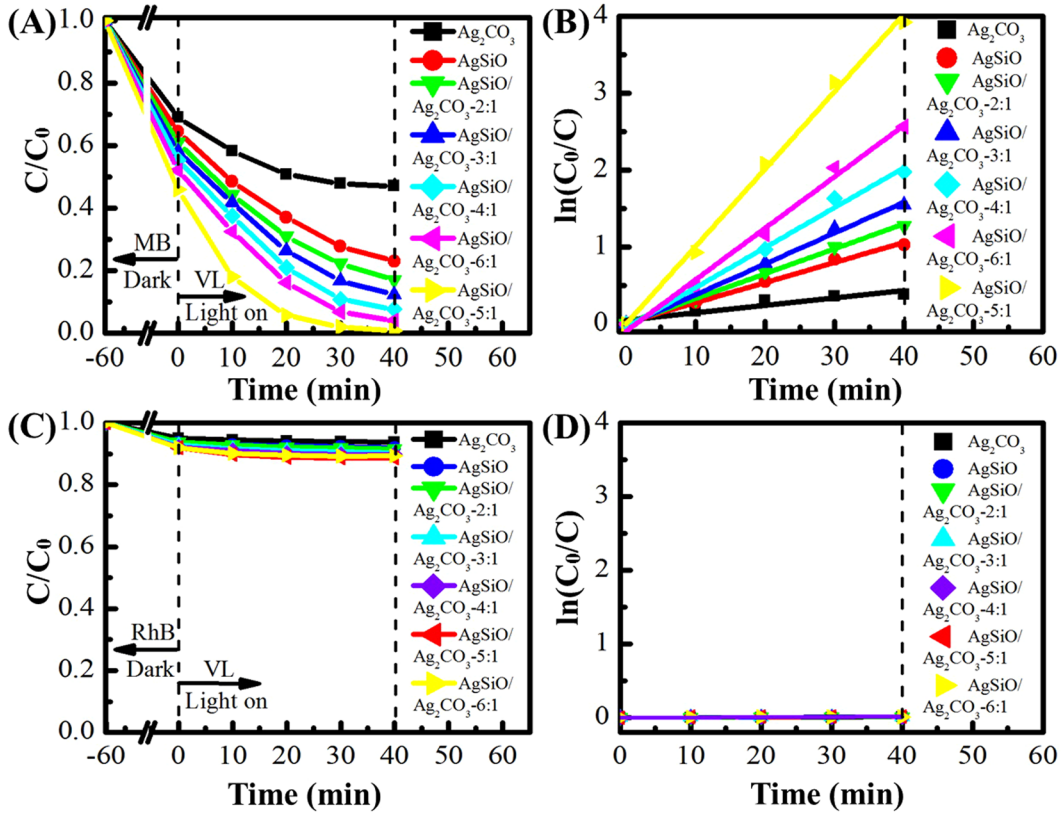

Figure 8. (**A**) The photocatalytic activities of the as-prepared photocatalysts for the degradation of MB under VL irradiation; (**B**) the rate constants of the as-prepared photocatalysts for the degradation of MB; (**C**) the photocatalytic activities of the as-prepared photocatalysts for the degradation of RhB under VL irradiation; (**D**) the rate constants of the as-prepared photocatalysts for the degradation of RhB.

anionic dyes remained unchanged[41]. These results demonstrated excellent selective removal of cationic dyes over anionic dyes due to the electrostatic effect[11,12].

Photocatalytic mechanism. The electrons and holes produced by photocatalysis have strong reduction and oxidation capacities. The main active species of different photocatalysts may vary due to their different band structure and phase compositions[10,38]. Thus, to explore the mechanism of the high photocatalytic activities and to assess the contribution of the reactive species, trapping experiments of reactive species were conducted using ethylenediaminetetraacetate (EDTA-2Na), iso-propyle alcohol (IPA) and N_2 as h^+ and OH^- and e^- scavengers, respectively[10,16]. By adding scavengers into the degradation solutions, the reactive species in the degradation process can be revealed. As shown in Fig. 10, the degradation rate decreases clearly to ~8.8% in the presence of EDTA-2Na (h^+ scavenger) and the degradation rate is ~98% in the absence of scavengers, which indicates that h^+ is the major reactive specie for MB degradation (Fig. 10A,B)[8,40]. Introducing IPA displays a significant effect on the K_{app}. It decrease from ~0.102 min^{-1} to ~0.055 min^{-1} (Fig. 10C), suggesting that the radical is also a dominant reactive species. And the degradation rate decreases obviously to ~53% and ~66% in the presence of N_2 (O^{2-} scavenger) and $AgNO_3$ (e^- scavenger), which suggests that O^{2-} and e^- is the partly reactive species for MB degradation (Fig. 10D,E). Through Fig. 10F, we can visually see that the O^{2-}, e^- and h^+ are reactive species[42].

The recyclability of the photocatalysts is significant factors in their practical applications. Figure 11A indicates that the recyclability for AgSiO/Ag_2CO_3-5:1 composite. After six successive cycles, AgSiO/Ag_2CO_3-5:1 composite still possesses ~89% degradation rate of MB after ~40 min VL irradiation, indicating its high recyclability[30,39,43]. The results indicate that the incorporation of AgSiO with Ag_2CO_3 photocatalyst successfully improves the VL photocatalytic performance and restrains the photocorrosion in a large level[13,44]. To further comprehend the separation and recombination of electron-hole pairs in pure AgSiO, Ag_2CO_3 and AgSiO/Ag_2CO_3 composites, the photocurrent test is carried out under visible light[33]. In this study, electrochemical and photoelectrochemical measurements were performed in 1 M Na_2SO_4 electrolyte solution in a three-electrode quartz cell. Pt sheet was used as a counter electrode and Hg/Hg_2Cl_2/sat. KCl was used as a reference electrode. The pure AgSiO, Ag_2CO_3 and AgSiO/Ag_2CO_3 composites on ITO was used as the working electrode for investigation. The photoelectrochemical response was recorded with a CHI 660E electrochemical system[33]. The photocurrent-potential plots of these samples are shown in Fig. 11B. The figure shows the obvious photocurrent intensity of different samples under illumination by 250 lumens LED for 30 second intervals. The best photocurrent intensity (0.7 $\mu A \cdot g^{-1}$) of AgSiO was obtained when the applied potential is 1.3 V. And the best photocurrent intensity of Ag_2CO_3 was 1.2 $\mu A \cdot g^{-1}$. However, the photocurrent intensity was improved to 1.8 $\mu A \cdot cm^{-1}$ with the same applied potential after

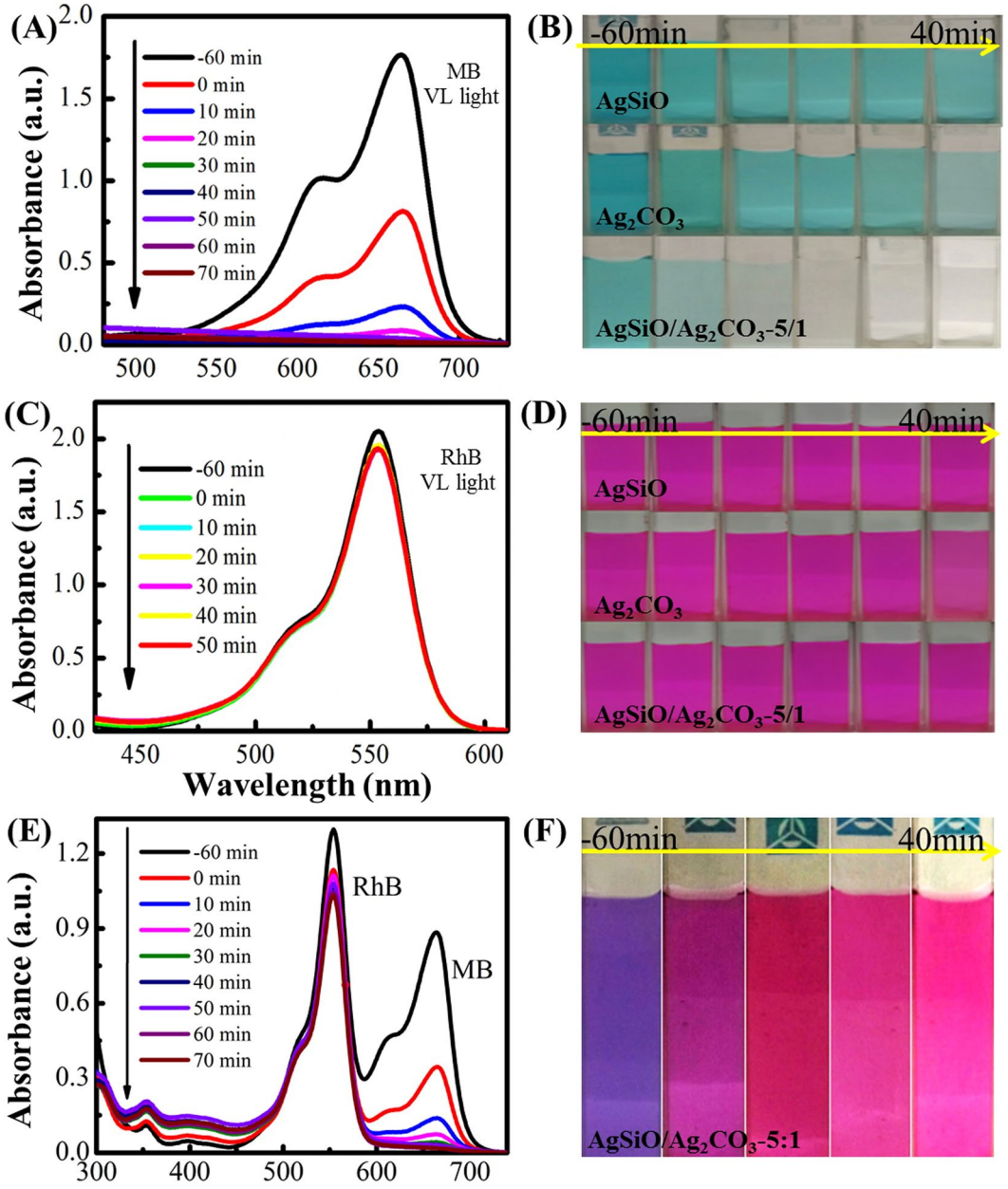

Figure 9. (**A**) The absorption spectra of MB degraded by AgSiO/Ag_2CO_3-5:1 composite under VL irradiation; (**B**) the corresponding digital photograph of MB degraded by AgSiO/Ag_2CO_3-5:1 composite under VL irradiation; (**C**) the absorption spectra of RhB degraded by AgSiO/Ag_2CO_3-5:1 composite under VL irradiation; (**D**) the corresponding digital photograph of RhB degraded by AgSiO/Ag_2CO_3-5:1 composite under VL irradiation; Absorption spectra (**E**) and corresponding digital photograph (**F**) of RhB and MB degraded by AgSiO/$AgCO_3$-5:1 composite under VL irradiation.

a heterojunction formed form AgSiO and Ag_2CO_3, which was three times greater than pure Ag_2CO_3. This phenomenon reveals that the AgSiO/Ag_2CO_3 heterostructures possess a larger carrier concentration than the pure AgSiO and Ag_2CO_3 NPs, and more electron-hole pairs are generated for the charge separation process[45]. These results of the photocurrent tests are in agreement with the results of the photodegradation of MB. The obvious photocurrent demonstrates that the interfacial charge separation between AgSiO and Ag_2CO_3 NPs exists in this composite[46].

Based on experimental results, Fig. 12 depicts a diagrammatic sketch for photocatalytic mechanism. Under VL irradiation, AgSiO can absorb VL, leading to the excitation of e^- to the conduction band (CB) and whilst keeping h^+ in the valence bands (VB)[2,7]. For AgSiO/Ag_2CO_3 heterojunctions, the photogenerated e^- on the CB of AgSiO can easily migrate to the CB of Ag_2CO_3 while the photogenerated h^+ in the VB of Ag_2CO_3 migrates to AgSiO[19]. That is to say, the appropriately aligned band edges of AgSiO and Ag_2CO_3 indicates that the migration of effective photogenerated charges can occur via the heterojunctions with strong interfacial coupling effect in

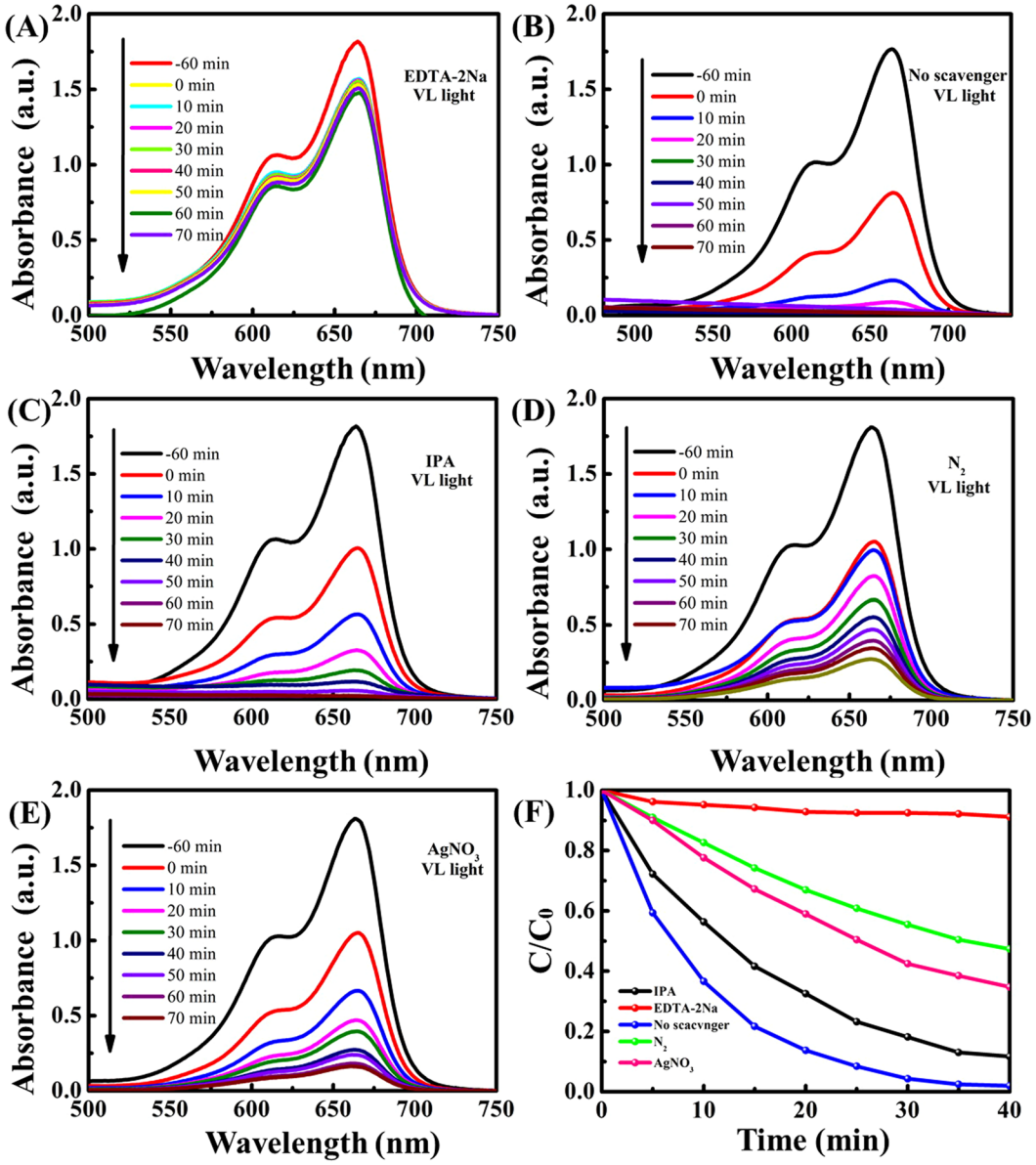

Figure 10. The typical visible absorption spectra (**A**–**E**) and concentration changes (**F**) of MB over AgSiO/Ag_2CO_3-5:1 composite in the presence of EDTA-2Na, IPA, N_2 and in the absence scavengers.

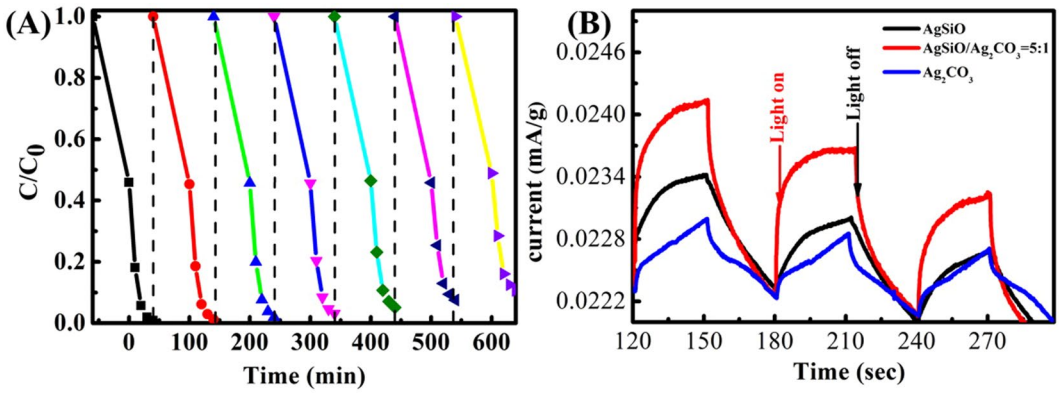

Figure 11. (**A**) The photocatalytic stability of AgSiO/Ag_2CO_3-5:1 composite in recycling reactions; Photocurrent response curves of pure Ag_2CO_3, AgSiO and AgSiO/Ag_2CO_3 composites under visible light irradiation (**B**).

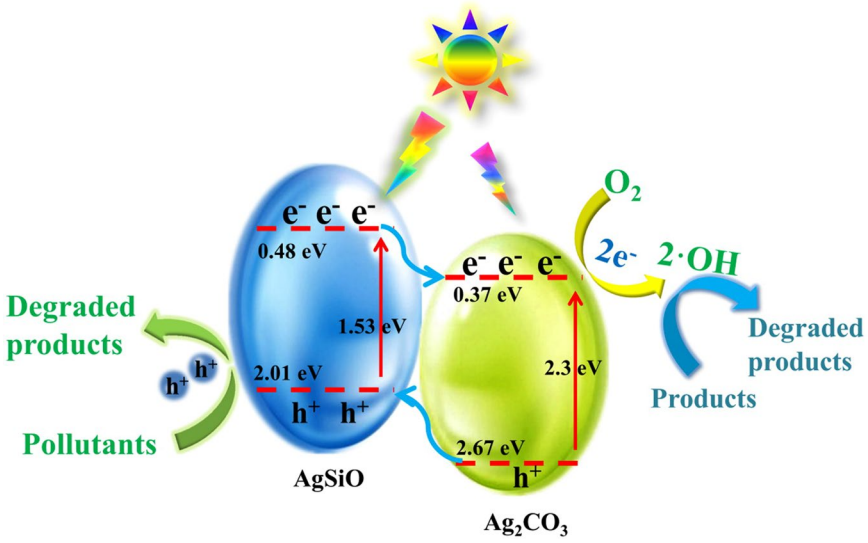

Figure 12. Proposed mechanisms of photogenerated charge transfer and pollutants degradation in the AgSiO/Ag_2CO_3-5:1 composite under VL irradiation.

the composite[47]. The migration of photogenerated charges limit the transmission of photogenerated e^- and h^+ on different sides, which reduces the recombination rate of photogenerated electron-hole pairs and improves the abundance and stability of photogenerated charge in the composite[6,7]. At the same time, the isolated photogenerated charges promote the production of reactive oxidative species, i.e. $\bullet O^{2-}$ and •OH, which are responsible for degrading MB confirmed by Fig. 12[26,48,49].

Conclusions

In summary, a facile *in-situ* precipitation method has been designed and developed to synthesize a series of AgSiO/Ag_2CO_3 composites with the sizes in the range of 100 nm. The as-synthesized AgSiO/Ag_2CO_3-5:1 composite shows superior VL photocatalytic activities, and the degradation of MB reach as ~99.1% under VL irradiation within ~40 min, which can be ascribed to the synergetic effect between AgSiO and Ag_2CO_3, including the maximum heterojunction interface with intimate contact, enhanced photogenerated charge separation efficiency, fully exposed reactive sites as well as excellent VL response in the composite. For the selectivity for degradation, we speculate that the discrepancy in degradation capacities among the two anionic dyes can be ascribed to the molecule size. This work will give insights into the importance of rational design of heterojunction systems, and provide a potential method for the construction of efficient heterojunction photocatalysts with controllable sizes and space distributions.

References

1. Shi, L., Liang, L., Wang, F., Liu, M. & Sun, J. Enhanced visible-light photocatalytic activity and stability over g-C_3N_4/Ag_2CO_3 composites. *J. Mater. Sci.* **50**, 1718–1727 (2015).
2. Li, Y. *et al.* Preparation and enhanced visible light photocatalytic activity of novel g-C_3N_4 nanosheets loaded with Ag_2CO_3 nanoparticles. *Nanoscale* **7**, 758–764 (2015).
3. Panthi, G. *et al.* Electrospun composite nanofibers of polyacrylonitrile and Ag_2CO_3 nanoparticles for visible light photocatalysis and antibacterial applications. *J. Mater. Sci.* **50**, 4477–4485 (2015).
4. Xu, X., Zhai, T., Shao, M. & Huang, J. Anodic formation of anatase TiO_2 nanotubes with rod-formed walls for photocatalysis and field emitters. *Phys. Chem. Chem. Phys.* **14**, 16371–16376 (2012).
5. Dai, G., Yu, J. & Liu, G. A new approach for photocorrosion inhibition of Ag_2CO_3 photocatalyst with highly visible-light-responsive reactivity. *J. Phy. Chem. C* **116**, 15519–15524 (2012).
6. Liu, J. *et al.* Anchoring of $Ag_6Si_2O_7$ nanoparticles on α-Fe_2O_3 short nanotubes as a Z-scheme photocatalyst for improving their photocatalytic performances. *Dalton T.* **45**, 12745–12755 (2016).
7. Lou, Z. *et al.* $Ag_6Si_2O_7$: a silicate photocatalyst for the visible region. *Chem. Mater.* **26**, 3873–3875 (2014).
8. Zhang, S. *et al.* Hybrid 0D-2D nanoheterostructures: *in-situ* growth of amorphous silver silicates dots on g-C_3N_4 nanosheets for full spectrum photocatalysis. *ACS Appl. Mater. Inter.* **8**, 35138–35149 (2016).
9. Zheng, Y., Lin, L., Ye, X., Guo, F. & Wang, X. Helical graphitic carbon nitrides with photocatalytic and optical activities. *Angew. Chem. Int. Edit.* **53**, 11926–11930 (2014).
10. Mehraj, O., Mir, N. A., Pirzada, B. M., Sabir, S. & Muneer, M. *In-situ* anion exchange synthesis of AgBr/Ag_2CO_3 hybrids with enhanced visible light photocatalytic activity and improved stability. *J. Mol. Catal. A: Chem.* **395**, 16–24 (2014).
11. Yang, H. *et al.* Constructing the novel ultrafine amorphous iron oxyhydroxide/g-C3N4 nanosheets heterojunctions for highly improved photocatalytic performance. *Sci. Rep.* **7**, 8686 (2017).
12. Shu, D., Feng, F., Han, H. & Ma, Z. Prominent adsorption performance of amino-functionalized ultra-light graphene aerogel for methyl orange and amaranth. *Chem. Eng. J.* **324**, 1–9 (2017).
13. Chen, F. *et al.* Novel ternary heterojunction photcocatalyst of Ag nanoparticles and g-C_3N_4 nanosheets co-modified $BiVO_4$ for wider spectrum visible-light photocatalytic degradation of refractory pollutant. *Appl. Catal. B: Environ.* **205**, 133–147 (2017).
14. Zhao, Q. *et al.* One-pot synthesis of Zn-doped SnO_2 nanosheet-based hierarchical architectures as a glycol gas sensor and photocatalyst. *CrystEngComm* **17**, 4394–4401 (2015).

15. Yu, C. *et al*. Enhancing the photocatalytic performance of commercial TiO_2 crystals by coupling with trace narrow-band-gap Ag_2CO_3. *Ind. Eng. Chem. Res.* **53**, 5759–5766 (2014).
16. Liu, L. *et al*. A stable Ag_3PO_4@ g-C_3N_4 hybrid core@ shell composite with enhanced visible light photocatalytic degradation. *Appl. Catal. B: Environ.* **183**, 133–141 (2016).
17. Han, S. W., Kim, Y. & Kim, K. Dodecanethiol-derivatized Au/Ag bimetallic nanoparticles: TEM, UV/VIS, XPS, and FTIR analysis. *J. Colloid Interf. SCI.* **208**, 272–278 (1998).
18. Kaushik, V. K. XPS core level spectra and Auger parameters for some silver compounds. *J. Electron Spectrosc.* **56**, 273–277 (1991).
19. Yu, C., Li, G., Kumar, S., Yang, K. & Jin, R. Phase transformation synthesis of novel Ag_2O/Ag_2CO_3 heterostructures with high visible light efficiency in photocatalytic degradation of pollutants. *Adv. Mater.* **26**, 892–898 (2014).
20. Epling, W. S., Hoflund, G. B. & Salaita, G. N. Surface characterization study of the thermal decomposition of Ag_2CO_3. *J. Phys. Chem. B* **102**, 2263–2268 (1998).
21. Dong, S. *et al*. Self-assembled hollow sphere shaped Bi_2WO_6/RGO composites for efficient sunlight-driven photocatalytic degradation of organic pollutants. *Chem. Eng. J.* **316**, 778–789 (2017).
22. Jin, X., Mok, E. K., Baek, J.-W., Park, S.-H. & Hwang, S.-J. Importance of the tuning of band position in optimizing the electronic coupling and photocatalytic activity of nanocomposite. *J. Solid State Chem.* **230**, 175–181 (2015).
23. Férey, G. *et al*. A chromium terephthalate-based solid with unusually large pore volumes and surface area. *Science* **309**, 2040–2042 (2005).
24. Sun, J. *et al*. Bioinspired hollow semiconductor nanospheres as photosynthetic nanoparticles. *Nat. Commun.* **3**, 1139 (2012).
25. Gaumet, M., Vargas, A., Gurny, R. & Delie, F. Nanoparticles for drug delivery: the need for precision in reporting particle size parameters. *Eur. J. Pharm. Biophar.* **69**, 1–9 (2008).
26. Fang, S. *et al*. Fabrication of BiOCl@ CdS/Ag_2CO_3 heterojunctions with enhanced photocatalytic activity under visible-light irradiation. *J. Mater. Sci.-Mater. El.* 1–9 (2017).
27. Al-Keisy, A. *et al*. A ferroelectric photocatalyst $Ag_{10}Si_4O_{13}$ with visible-light photooxidation properties. *J. Mater. Chem. A* **4**, 10992–10999 (2016).
28. Yang, M.-Q. *et al*. Self-surface charge exfoliation and electrostatically coordinated 2D hetero-layered hybrids. *Nat. Commun.* **8**, 14224 (2017).
29. Yu, C.-L. *et al*. Novel AgCl/Ag_2CO_3 heterostructured photocatalysts with enhanced photocatalytic performance. *Rare Metals* **35**, 475–480 (2016).
30. Yu, B. *et al*. Preparation of electrospun Ag/g-C_3N_4 loaded composite carbon nanofibers for catalytic applications. *Mater. Res. Express* **4**, 1 (2017).
31. Zhu, X. *et al*. Synthesis of novel visible light response $Ag_{10}Si_4O_{13}$ photocatalyst. *Appl. Catal. B: Environ.* **199**, 315–322 (2016).
32. Chen, Q., Wu, S. & Xin, Y. Synthesis of Au-CuS-TiO_2 nanobelts photocatalyst for efficient photocatalytic degradation of antibiotic oxytetracycline. *Chem. Eng. J.* **302**, 377–387 (2016).
33. Yang, M.-Q. *et al*. Ultrathin nickel boron oxide nanosheets assembled vertically on graphene: a new hybrid 2D material for enhanced photo/electro-catalysis. *Mater. Horiz.* **4**, 885–894 (2017).
34. Liu, J. *et al*. 2D ZnO mesoporous single-crystal nanosheets with exposed {0001} polar facets for the depollution of cationic dye molecules by highly selective adsorption and photocatalytic decomposition. *Appl. Catal. B: Environ.* **181**, 138–145 (2016).
35. Yao, Z. *et al*. Preparation, characterization, and antibacterial activity of shell waste loaded with silver. *J. Mater. Sci.* **48**, 8580–8587 (2013).
36. Cui, W. *et al*. Microwave-assisted synthesis of Ag@AgBr-intercalated $K_4Nb_6O_{17}$ composite and enhanced photocatalytic degradation of Rhodamine B under visible light. *Chem. Eng. J.* **230**, 10–18 (2013).
37. Hou, R. *et al*. Coupling system of Ag/BiOBr photocatalysis and direct contact membrane distillation for complete purification of N-containing dye wastewater. *Chem. Eng. J.* **317**, 386–393 (2017).
38. Shu, J. *et al*. One-pot synthesis of AgCl@ Ag hybrid photocatalyst with high photocatalytic activity and photostability under visible light and sunlight irradiation. *Chem. Eng. J.* **252**, 374–381 (2014).
39. Ma, X. *et al*. Comparison of photocatalytic reaction-induced selective corrosion with photocorrosion: Impact on morphology and stability of Ag-ZnO. *Appl. Catal. B: Environ.* **201**, 348–358 (2017).
40. Orge, C., Pereira, M. & Faria, J. Photocatalytic-assisted ozone degradation of metolachlor aqueous solution. *Chem. Eng. J.* **318**, 247–253 (2017).
41. Liang, H., Jia, Z., Zhang, H., Wang, X. & Wang, J. Photocatalysis oxidation activity regulation of Ag/TiO_2 composites evaluated by the selective oxidation of Rhodamine B. *Appl. Surf. Sci.* **422**, 1–10 (2017).
42. Suyana, P. *et al*. Co_3O_4-C_3N_4 p-n nano-heterojunctions for the simultaneous degradation of a mixture of pollutants under solar irradiation. Environ. *Sci. Nano.* **4**, 212–221 (2017).
43. Zhang, D., Li, J., Wang, Q. & Wu, Q. High {001} facets dominated BiOBr lamellas: facile hydrolysis preparation and selective visible-light photocatalytic activity. *J. Mol. Catal. A* **1**, 8622–8629 (2013).
44. Gou, W., Wu, P., Jiang, D. & Ma, X. Synthesis of AgBr@ Bi_2O_3 composite with enhanced photocatalytic performance under visible light. *J. Alloy. Compd.* **646**, 437–445 (2015).
45. Han, C., Quan, Q., Chen, H. M., Sun, Y. & Xu, Y. J. Progressive Design of Plasmonic Metal-Semiconductor Ensemble toward Regulated Charge Flow and Improved Vis-NIR-Driven Solar-to-Chemical Conversion. *Small* **13**, 14 (2017).
46. Xu, K. *et al*. Ag-CuO-ZnO metal-semiconductor multiconcentric nanotubes for achieving superior and perdurable photodegradation. *Nanoscale* **9**, 11574–11583 (2017).
47. Chen, F. *et al*. Facile preparation of ternary Ag_2CO_3/Ag/PANI composite nanorods with enhanced photoactivity and stability. *J. Mater. Sci.* **52**, 4521–4531 (2017).
48. Zhang, P. *et al*. Synthesis of sandwich-structured AgBr@Ag@TiO_2 composite photocatalyst and study of its photocatalytic performance for the oxidation of benzyl alcohols to benzaldehydes. *Chem. Eng. J.* **306**, 1151–1161 (2016).
49. Yang, M.-Q., Zhang, N., Wang, Y. & Xu, Y.-J. Metal-free, robust, and regenerable 3D graphene–organics aerogel with high and stable photosensitization efficiency. *J. Catal.* **346**, 21–29 (2017).

Acknowledgements

Financial supports from NSFC (Grant Nos 51672109, 21505050) and the Natural Science Foundation of Shandong Province (Grant No. ZR2016JL015, ZR2016FM30).

Author Contributions

C.R.Y. performed the experiments. D.X.L. and Y.H.C. performed the SEM observations and TEM observations. Z.S.W. and X.X.J. discussed and commented on the experiments and results, and wrote the paper.

Additional Information

Supplementary information accompanies this paper at https://doi.org/10.1038/s41598-017-15405-6.

Competing Interests: The authors declare that they have no competing interests.